Hindawi
International Journal of Antennas and Propagation
Volume 2022, Article ID 8287435, 9 pages
https://doi.org/10.1155/2022/8287435

Research Article

The Incident Field Optimization Method for the Electromagnetic Inverse Problems

Hao Li, Lijia Chen, and Jinghui Qiu

Microwave Engineering Department, Harbin Institute of Technology, Harbin, China

Correspondence should be addressed to Lijia Chen; ljchen@hit.edu.cn

Received 20 September 2021; Accepted 22 April 2022; Published 25 May 2022

Academic Editor: Miguel Ferrando Bataller

In this letter, an incident field optimization (IO) method integrated with contrast source inversion (CSI) method and multiplicative regularized CSI (MR-CSI) method is proposed to deal with the electromagnetic inverse problems. For the conventional iterative inversion methods, the incident field is a prior knowledge and is usually obtained by the calibration process. Through the synthetic data experiments, it can be found that a small distortion of the incident field has little impact on the inversion results, but a high distortion will lead to fault inversion results or no convergence. In this letter, the incident field optimal factor, being updated during the iterative process, is introduced into the CSI and MR-CSI method, named as IO-CSI and MR–IO–CSI. The new methods have good inversion performance even with high incident field distortion. The proposed methods are applied to the Fresnel experiment data directly without the calibration procedure. Both the single-frequency and multifrequency inversion experiments demonstrate that the IO-CSI and MR–IO–CSI method can achieve good inversion results, indicating the method's practical applicability.

1. Introduction

For the electromagnetic inverse scattering problem, the task is to reconstruct the permittivity or conductivity distribution in the domain of interest (DOI) by the measured scattered field. The contrast source inversion (CSI) method is one of the outstanding frequency domain iterative methods to solve the inverse problem by minimizing the cost function, which is a linear combination of normalized mismatches between the data equation and the state equation. Since its proposition [1, 2], the CSI method has become very popular and many transformations have been developed. In [3], a multiplicative regularized inversion scheme of CSI was proposed and the artificial weighting parameter is avoided. In [4, 5], a new integral equation was introduced which can solve the inverse problem with high contrast. In [6, 7], a subspace-based optimization method (SOM) was invented, in which the induced current is divided into two parts, major and minor parts, to reduce the computational burden and to improve the inversion result. In [8, 9], the authors added cross-correlated error into the final cost function, forming the cross-correlated contrast source inversion (CC–CSI) method, which can achieve good robustness and higher inversion accuracy. To deal with the nonhomogeneous background inverse problem, the finite-difference frequency domain (FDFD)-based CSI [10, 11] and finite-element method (FEM)-based CSI [12, 13] were proposed, extending the application scenario of the CSI method. Recently, the deep learning (DL) method was introduced to solve the multifrequency electromagnetic inverse problems [14].

Usually, in these methods, the true incident field is known as the prior information or obtained by a certain calibration factor, which is derived from the ratio of the measured incident field to the simulated one at the receiver located at the opposite of the source [15, 16]. Ostadrahimi et al. [17] used the scattered field for calibration. Narendra et al. [18] adopted the source reconstruction method to achieve more stable inversion results. The incident field was represented by a superposition of a few cylindrical waves in [19]. In [20], an incident-modified CSI method is proposed to design the artificial material.

Although it is better to perform the incident field calibration in order to start the iterative inversion algorithm with the most accurate information that is available, in reality the incident field cannot be obtained precisely. Therefore, it is necessary to study the influence of incident field distortion on the inversion results. The incident field optimization method, cooperating with contrast source inversion (CSI) method and multiplicative regularized CSI (MR-CSI) method, is proposed in this paper. The incident field calibration factor is treated as an optimization factor that is updated during each iteration step and the incident field will converge to its true value.

The IO-CSI and MR-IO-CSI methods are applied to the Fresnel-measured data where the initial incident field is the unit line source. It is shown that the methods have a very good performance even though the initial guess of back propagation (BP) inversion result has distortions because of the incorrect incident field information. For the multifrequency inversion experiment, the conventional CSI has failed to reconstruct the targets while the IO inversion methods can still converge to the true value.

The letter is organized as follows: Section 2 is the formulation of the problem. The incident field optimization CSI (IO–CSI) method and multiplicative regularized IO-CSI (MR-IO-CSI) method are introduced in Section 3. In Section 4, the synthetic and measured data inverse experiments at single and multiple frequencies are carried out. Section 5 is the conclusion.

2. Materials and Methods

2.1. Electromagnetic Inverse Problem Configuration. The configuration of a simple two-dimensional (2D) electromagnetic scattering inverse problem is shown in Figure 1. The domain of interest (DOI) D containing unknown scatterers, characterized by $\varepsilon_r(\mathbf{r})$, is illuminated by incoming waves $E^{\text{inc}}_{n,k}$ generated by nth ($n = 1 \ldots \text{N}$) transmitter at kth ($k = 1 \ldots \text{K}$) measurement frequency, while the scattered field is measured by M receivers located in the measurement domain S around the domain D.

For transverse magnetic (TM) cases, the forward problem is described by two equations:

$$E^{\text{tot}}_{n,k}(\mathbf{r}) = E^{\text{inc}}_{n,k}(\mathbf{r}) + k^2_{0,k}\int_D g_k(\mathbf{r}, r')\chi_k(r')E^{\text{tot}}_{n,k}(r') \text{ for } \mathbf{r} \in \text{D},$$
$$E^{\text{sca}}_{n,k}(\mathbf{r}) = k^2_{0,k}\int_D g_k(\mathbf{r}, r')\chi_k(r')E^{\text{tot}}_{n,k}(r') \text{ for } \mathbf{r} \in \text{S}, \tag{1}$$

where the first one is the state equation and the second one is the data equation, $E^{\text{tot}}_{n,k}(\mathbf{r})$ is the total electric wave field, $E^{\text{inc}}_{n,k}(\mathbf{r})$ is the incident field, $k_{0,k} = \omega\sqrt{\mu_0\varepsilon_0}$ is the wavenumber of the homogeneous background medium at kth frequency, and $g_k(\mathbf{r}, r')$ is Green's function. The contrast $\chi_k(\mathbf{r})$ is defined as

$$\chi_k(\mathbf{r}) = \frac{\varepsilon_r(\mathbf{r}) - \varepsilon_0}{\varepsilon_0} - j\frac{\sigma(\mathbf{r})}{\omega_k\varepsilon_0}, \tag{2}$$

where $j = \sqrt{-1}$. For the inverse scattering problems, the task is to reconstruct $\varepsilon_r(\mathbf{r})$ by the measured scattered field $E^{\text{sca}}_{n,k}(\mathbf{r})$ at receiver locations.

2.2. Contrast Source Inversion Method. The cost function of CSI method is

$$f_{\text{CSI}}\left(J_{n,k}, \chi_k\right) = \sum_k \frac{\sum_{n=1}^N \left\|E^{\text{sct}}_{n,k} - G^S_k\left(J_{n,k}\right)\right\|^2_S}{\sum_{n=1}^N \left\|E^{\text{sct}}_{n,k}\right\|^2_S} + \sum_k \frac{\sum_{n=1}^N \left\|\chi_k E^{\text{inc}}_{n,k} + \chi_k G^D_k\left(J_{n,k}\right) - J_{n,k}\right\|^2_D}{\sum_{n=1}^N \left\|\chi_k E^{\text{inc}}_{n,k}\right\|^2_D}. \tag{3}$$

The first term is the normalized data error, contributing from the mismatch of the data equation, and the second term is the normalized state error due to the mismatch of the state equation. $_S$ and $_D$ denote the Euclidian length of the function defined in domain S and domain D. The induced current $J_{n,k}$ and the contrast χ_k are updated alternatively during each iteration.

Usually, the back propagation method is used for the initial guess, the initial contrast source is

$$J^0_{n,k}(\mathbf{r}) = \frac{\langle E^{\text{sct}}_{n,k}, G^S_k\left(G^{S*}_k\left(E^{\text{sct}}_{n,k}\right)\right)\rangle_S}{\left\|G^S_k\left(G^{S*}_k\left(E^{\text{sct}}_{n,k}\right)\right)\right\|_{S^2}} G^{S*}_k\left(E^{\text{sct}}_{n,k}\right), \tag{4}$$

where $\langle\,\rangle_S$ denotes the inner product of functions in domain S and the initial contrast is

$$\chi^0_1(\mathbf{r}) = \frac{\text{Re}\left(\sum_k\sum_n J^0_{n,k}(\mathbf{r}) \cdot \left[E^{\text{tot},0}_{n,k}(\mathbf{r})\right]^*\right)}{\sum_k\sum_n\left|E^{\text{tot},0}_{n,k}(\mathbf{r})\right|^2} + j\frac{\text{Im}\left(\sum_k(\omega_1/\omega_k)\sum_n J^0_{n,k}(\mathbf{r}) \cdot \left[E^{\text{tot},0}_{n,k}(\mathbf{r})\right]^*\right)}{\sum_k(\omega_1/\omega_k)^2\sum_n\left|E^{\text{tot},0}_{n,k}(\mathbf{r})\right|^2}, \tag{5}$$

where $E^{\text{tot},0}_{n,k}(\mathbf{r}) = E^{\text{inc},0}_{n,k}(\mathbf{r}) + G^D_k(J^0_{n,k})$.

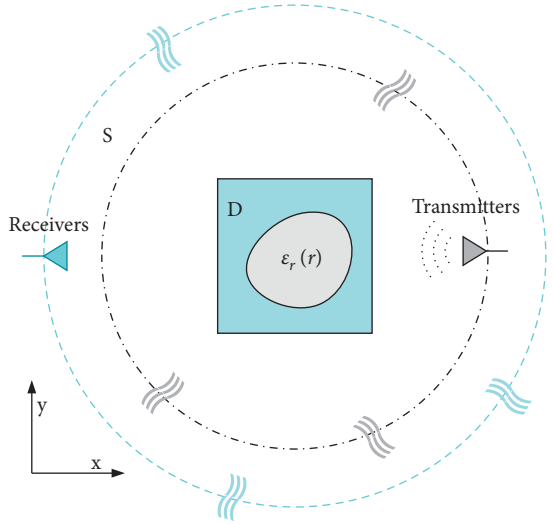

Figure 1: The configuration of the electromagnetic inverse problem.

2.3. Incident Field Optimization Method. For the conventional iterative inversion methods, the calibration factor is derived from the calibration procedure by data preprocessing. For the IO-CSI method, the calibration factor was treated as an optimization factor α, which is updated during each iteration. So, the cost function, with the change of $\mathbf{E}_n^{\text{inc}} \longrightarrow \alpha \mathbf{E}_n^{\text{inc}}$ in the second term of (3), can be rewritten as follows:

$$f_{\text{IO-CSI}}\left(J_{n,k}, \chi_k\right) = \sum_k \frac{\sum_{n=1}^{N} \left\| \mathbf{E}_{n,k}^{\text{sct}} - G_k^S\left(J_{n,k}\right) \right\|_S^2}{\sum_{n=1}^{N} \left\| \mathbf{E}_{n,k}^{\text{sct}} \right\|_S^2} + \sum_k \frac{\sum_{n=1}^{N} \left\| \chi_k\left(\alpha_k \mathbf{E}_{n,k}^{\text{inc}}\right) + \chi_k G_k^D\left(J_{n,k}\right) - J_{n,k} \right\|_D^2}{\sum_{n=1}^{N} \left\| \chi_k\left(\alpha_k \mathbf{E}_{n,k}^{inc}\right) \right\|_D^2}. \tag{6}$$

For the two-dimension (2D) case, the initial guess of the incident field can be chosen from the line sources parallel to the z-axial or plane waves, $\mathbf{E}^{\text{inc}}$. The initial optimization factor is $\alpha_k^0 = 1$. For the TM case, the incident field can be modelled as follows:

$$\begin{aligned} \mathbf{E}_{n,k}^{\text{inc},0} &= E_0 \frac{j}{4} H_0^{(1)}\left(k_{0,k} \left| \mathbf{r}_n - r' \right|\right) \text{ for } \mathbf{r}_n \in D \\ &= \alpha_k^0 \frac{j}{4} H_0^{(1)}\left(k_{0,k} \left| \mathbf{r}_n - r' \right|\right) \text{ for } \mathbf{r}_n \in D. \end{aligned} \tag{7}$$

where $H_0^{(1)}$ is the zeroth-order Hankel function of the first kind, r' is the source location. The optimization factor is updated at each iteration by minimizing the numerator of the second term of the (6):

$$\min : f\left(\alpha_k\right) = \sum_{n=1}^{N} \left\| \chi_k\left(\alpha_k E_n^{\text{inc}}\right) + \chi_k G_k^D\left(J_{n,k}\right) - J_{n,k} \right\|_D^2. \tag{8}$$

The implementation steps of the IO-CSI method are shown in Algorithm 1.

The method is also applied to the multiplicative regularized CSI, named MR-IO-CSI, which has the same update steps as the IO-CSI method. The cost function is given by

$$f_{\text{MR-IO-CSI}}\left(J_{n,k}^i, \chi_k^i\right) = f_{\text{IO-CSI}}\left(J_{n,k}^i, \chi_k^i\right) \cdot \frac{1}{V} \int_D \frac{\left|\nabla \chi\left(\mathbf{r}\right)\right|^2 + \delta_{i-1}^2}{\left|\nabla \chi_{i-1}\left(\mathbf{r}\right)\right|^2 + \delta_{i-1}^2} \, \mathrm{d}v\left(\mathbf{r}\right), \tag{9}$$

where δ_{i-1}^2 is defined as

$$\delta_{i-1}^2 = \frac{1}{\Delta^2} \frac{\left\| \mathbf{E}^{\text{sct}} - \mathbf{G}\left(\mathbf{J}^{i-1}\right) \right\|_S^2}{\left\| \mathbf{E}^{\text{sct}} \right\|_S^2}, \tag{10}$$

where $V = \int_D \mathrm{d}v\left(\mathbf{r}\right)$ is the area of the domain D and Δ is the mesh size of the discretized domain D. The optimization will be terminated if the termination condition (the maximum iteration is reached or the residual value does not change obviously) is satisfied.

3. Results and Discussion

In this letter, the scatterers are lossless so that their permittivity is positive and conductivity equals zero. The background is the free space, so its relative permittivity equals 1.

Algorithm steps:
1: Obtain the $J_{n,k}^0(\mathbf{r})$ and $\chi_k^0(\mathbf{r})$ by the BP method.
2: Update $J_{n,k}^i(\mathbf{r})$ using the conjugate gradient (CG) method.
3: Update α_k^i: $\alpha_k^i = (-\sum_{n=1}^N (\chi_k^{i-1}\mathbf{E}_{n,k}^{\mathrm{inc},i-1})^* [G_k^D(\chi_k^{i-1}\mathbf{E}_{n,k}^{\mathrm{tot},i-1}) - J_{n,k}^i]/\sum_{n=1}^N \|\chi_k^{i-1}\mathbf{E}_{n,k}^{\mathrm{inc},i-1}\|^2)$.
4: Update incident filed $\mathbf{E}_{n,k}^{\mathrm{inc},i}$ and total field $\mathbf{E}_{n,k}^{\mathrm{tot},i}$ in DOI.
5: Update $\chi_k^i(\mathbf{r})$.
6: If meet the terminate condition, stop iteration and output the final result; otherwise, go to step 2.

Algorithm 1: Implementation steps of the IO-CSI method.

3.1. The Synthetic Experiment of Austria Profile. As shown in Figure 2(a), the 'Austria' profile consists of two discs and one ring. In the electromagnetic simulation, 16 line sources and 32 line receivers are evenly placed on circles with a radius of 3 m, using the method of moment (MoM) to simulate the scattered field at frequency 400 MHz. 100×100 grid mesh is used in the forward problem to generate the scattered data and the grid mesh is 64×64 in the inverse problem. Figure 2(b) gives the original CSI result with the true incident field.

To show the influence of the incident field distortion on the performance of the CSI method, the scattered field was obtained under different incident field amplitudes as $E_{in} = 0.5, 2, -2, 0.5j, 1 + 1j$, and $2j$ in the forward simulation processes. In the inversion stage of CSI, the calibration factor was set to $\alpha = 1$ without optimization. Some inversion results are shown in Figure 3. It can be seen that the shape and relative permittivity of the 'Austria' profile were reconstructed with some noise in Figure 3(b) ($E_{in} = 1.5$) and Figure 3(c) ($E_{in} = 2$), while the inversion results of Figure 3(a) ($E_{in} = 0.5$) and Figure 3(d) ($E_{in} = -2j$) have big distortion, making them unrecognizable.

Figure 4 is the inversion result of the IO-CSI method with 1000 iterations. Figure 4(a) is the curve of the optimization factor α under different incident field amplitude E_{in}. Starting from $\alpha_0 = 1$, the optimization factor is converged to the corresponding true value of the incident field under all conditions. Figure 4(b) is the IO-CSI inversion result, which is very similar to Figure 2(b) that is the original CSI result with the true incident field and the exact scatterers.

3.2. The Fresnel Measurement Data. The profile of the Fresnel experiment [16] is shown in Figure 5. The small circle represents a plastic cylinder (berylon) with a diameter of 31 mm and relative permittivity of $\varepsilon_r = 3 \pm 0.3$. The large circle represents a foam cylinder (SAITEC SBF 300) with a diameter of 80 mm and relative permittivity of $\varepsilon_r = 1.45 \pm 0.15$. The 8 transmitting antennas and 241 receiving antennas are all wideband ridged horn antennas with a frequency range from 1 to 18 GHz. The source-object center and object center-receiver distances are 1.67 m. Every target can be included in a $0.15 \times 0.15\,\mathrm{m}^2$ square centered at the center of the receiver circle. In this letter, only the TM data at 3 GHz and 5 GHz has been considered and the size of domain D is $0.18 \times 0.18\,\mathrm{m}^2$ which is discretized into 64×64 pixels.

In this inversion problem, the termination condition is the value of the cost function below the 10^{-3}. The iteration times are shown in Table 1, the MR-IO-CSI and IO-CSI need more iteration steps to meet the condition compared to the MR-CSI and CSI because of the introduction of the optimization factor.

The inversion results of 'FoamDielExtTM,' 'FoamDielIntTM,' and 'FoamTwinDielTM' at 3 GHz and 5 GHz are shown in Figures 6 and 7. Figures 6(a) and 7(a) is the BP results with the incident field initialized by equation (13) as $\alpha_0 = 1$. The BP results nearly have no similarity with the original profile of the targets. After several iterations, with the optimization factor converging to the true amplitude of the incident field, the MR-IO-CSI method successfully reconstructed the targets with a good match of shape and relative permittivity, as shown in Figures 6(b) and 7(b) at 3 GHz and 5 GHz. Figures 6(c) and 7(c) are the IO-CSI results also at 3 GHz and 5 GHz. It can be seen that the reconstructed images have some distortion, but each cylinder is still clearly shown in all cases.

The experiments show that both MR-IO-CSI and IO-CSI can solve the electromagnetic inverse problem without the prior knowledge of the incident field, and the MR-IO-CSI method has better performance than that of the IO-CSI method.

3.3. Multifrequency Inversion. In this part, the multifrequency datasets of 'FoamDielExtTM,' 'FoamDielIntTM,' and 'FoamTwinDielTM' at 5 GHz, 6 GHz, 7 GHz, and 8 GHz are processed by the multifrequency IO-CSI method and multifrequency MR-IO-CSI method. The iterations stop after 1500 steps.

The computation times of each method are shown in Table 2. Because of the incident field optimization process, the computation times of IO-CSI and MR-IO-CSI are longer than those of CSI and MR-CSI.

The CSI (the first row) and IO-CSI (the second row) results are shown in Figure 8. The CSI results show that the reconstructed relativity permittivity of small target is higher than the true value and the shape of the big target is neglected in 'FoamDielIntTM' and 'FoamTwinDielTM' cases where the two types of target are overlapping. However, the IO-CSI method retrieve the shape and relativity permittivity of the targets more correctly in all cases, even though the initial guess is distorted because of the incorrect initial incident field.

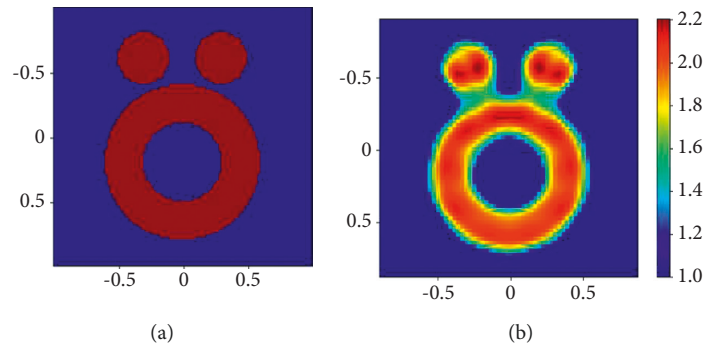

FIGURE 2: (a) The exact profile of the 'Austria' and (b) original CSI inversion result of the relative permittivity $\varepsilon_r = 2$ of 'Austria' at frequency of 400 MHz.

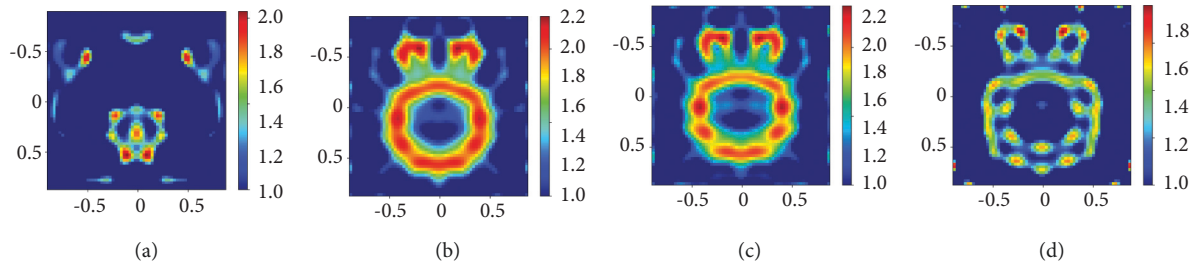

FIGURE 3: The CSI inversion results of the Austria profile with $\varepsilon_r = 2$ with the calibration factor $\alpha = 1$ in inversion stage, with $E_{in} = 0.5$ (a), 1.5 (b), 2 (c), and −2i (d) in the forward simulation. (a)$E_{\text{in}} = 0.5$. (b)$E_{\text{in}} = 1.5$. (c)$E_{\text{in}} = 2$. (d)$E_{in} = -2j$.

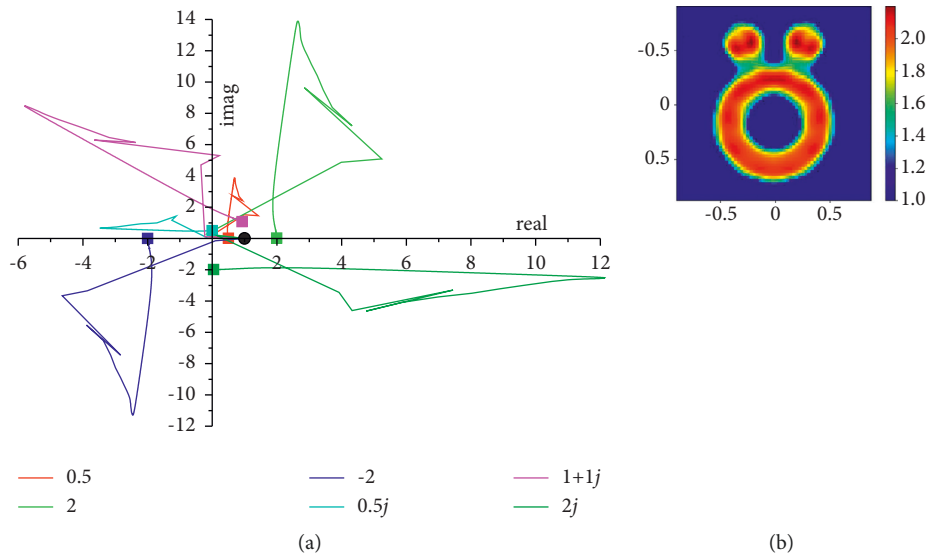

FIGURE 4: (a) Curve of the optimization factor in IO-CSI. The horizontal axis is the real part and the vertical axis is the imaginary part. For each curve, the black dot is the starting point and the square point is the ending point. And (b) IO-CSI inversion result.

The MR-CSI (the first row) and MR-IO-CSI (the second row) inversion results are shown in Figure 9. Both methods have good performance in the 'FoamDielExtTM' case (Figure 9(a)). In the right two cases (Figures 9(b) and 9(c)), the MR-CSI method has failed to retrieve the targets, but the MR-IO-CSI method successfully reconstructs the shape and relativity permittivity of all targets.

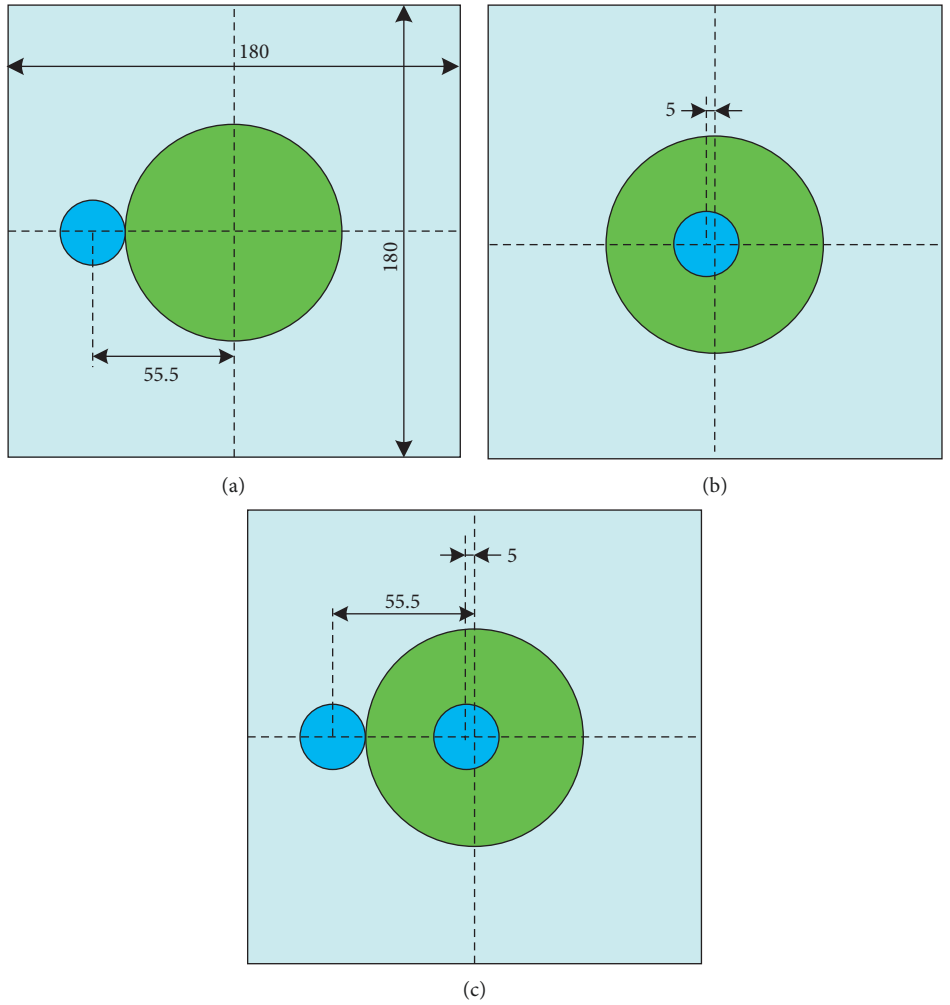

Figure 5: The targets used in the Fresnel experiments (dimension in mm): (a) FoamDielExt, (b) FoamDielInt, and (c) FoamTwinDiel. The small blue circle is plastic cylinder with relative permittivity $\varepsilon_r = 3 \pm 0.3$ and the radius of 15.5 mm; the large green circle is foam cylinder with relative permittivity $\varepsilon_r = 1.45 \pm 0.15$ and radius of 40 mm.

Table 1: The iteration times for different methods.

Item	MR-IO-CSI	MR-CSI	IO-CSI	CSI
FoamDielExtTM 3G	276	125	550	135
FoamDielExtTM 5G	168	97	292	180
FoamDielIntTM 3G	731	65	693	73
FoamDielIntTM 5G	214	16	372	121
FoamTwinDielTM 3G	188	85	742	82
FoamTwinDielTM 5G	180	134	501	227

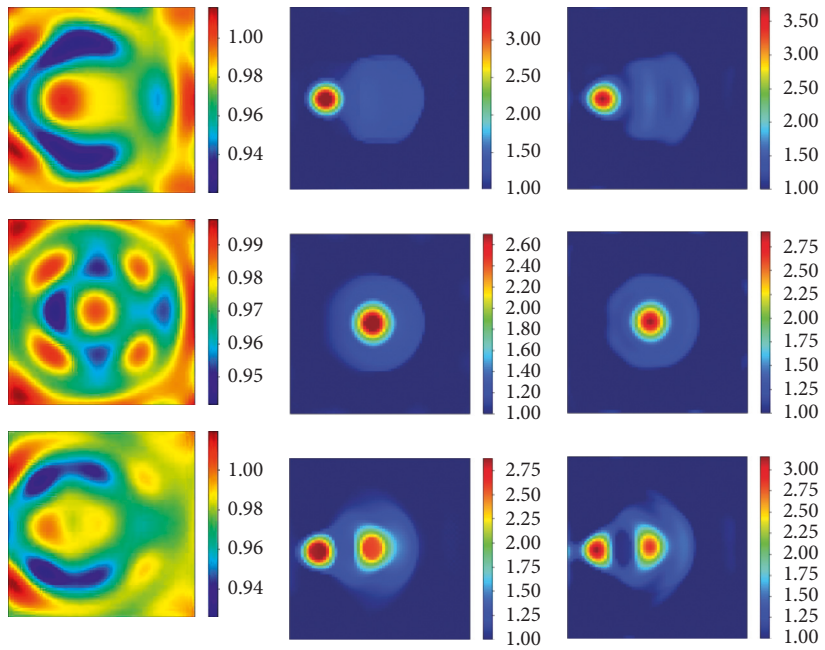

FIGURE 6: From top to bottom is the inversion results of 'FoamDielExtTM,' 'FoamDielIntTM,' 'FoamTwinDielTM' at 3 GHz. (a) is the BP results, (b) is the MR–IO– CSI results, and (c) is the IO-CSI results.

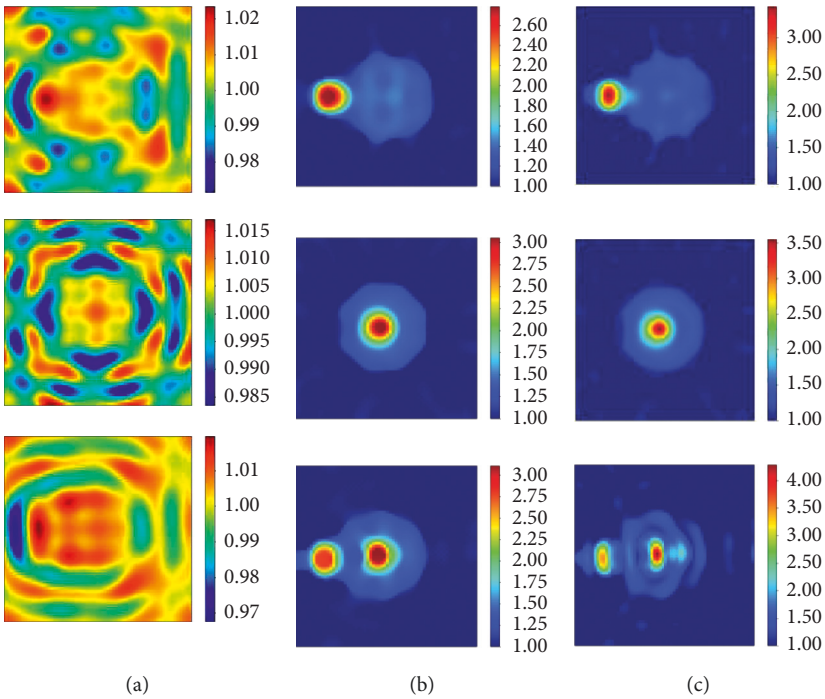

FIGURE 7: From top to bottom is the inversion results of 'FoamDielExtTM,' 'FoamDielIntTM,' 'FoamTwinDielTM' at 5 GHz. (a) is the BP results, (b) is the MR-IO-CSI results, and (c) is the IO-CSI results.

Table 2: The comparison of computation times (second).

Item	CSI	IO-CSI	MR-CSI	MR-IO-CSI
FoamDielExtTM	2182.2	3234.0	2359.2	3285.7
FoamDielIntTM	2186.3	3208.8	2268.2	3251.7
FoamTwinDielTM	2329.8	3657.9	2399.2	3548.7

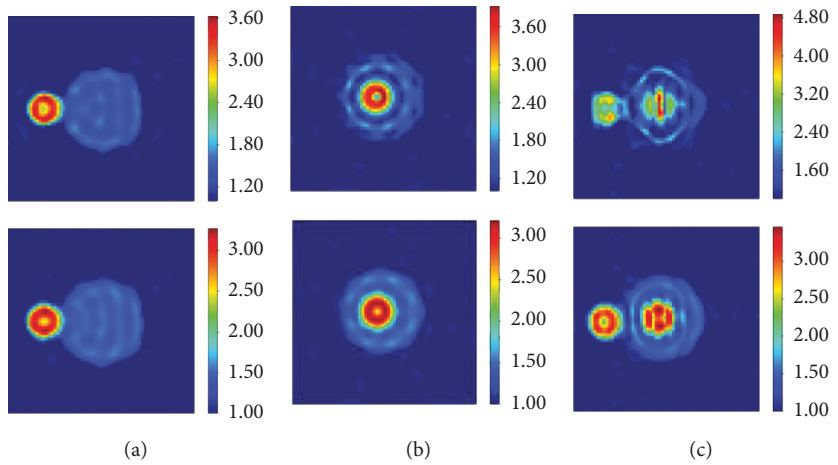

Figure 8: The multifrequency CSI inversion results (first row) and the multifrequency IO-CSI inversion results (second row) of (a) 'FoamDielExtTM,' (b) 'FoamDielIntTM,' and (c) 'FoamTwinDielTM' at 5 GHz, 6 GHz, 7 GHz, and 8 GHz.

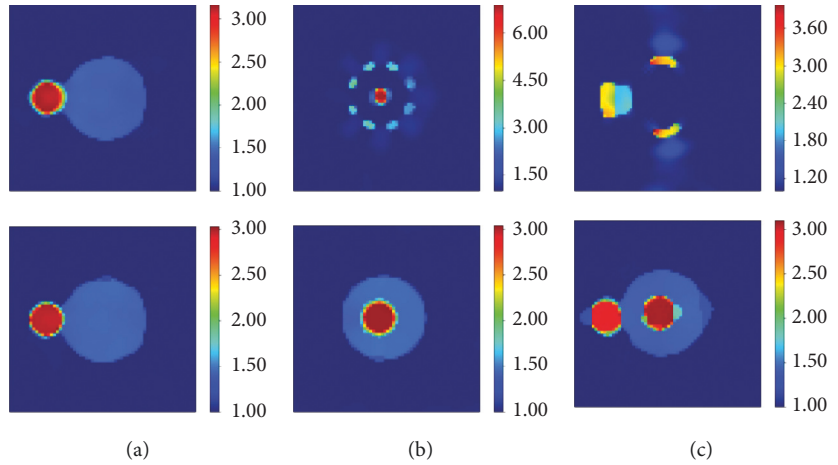

Figure 9: The multifrequency MR-CSI inversion results (first row) and the multifrequency MR-IO-CSI inversion results (second row) of (a) 'FoamDielExtTM,' (b) 'FoamDielIntTM,' and (c) 'FoamTwinDielTM' at 5 GHz, 6 GHz, 7 GHz, and 8 GHz.

4. Conclusions

In this letter, the incident field optimization factor is used to replace the calibration factor in the electromagnetic inverse problems. Through the synthetic data inverse experiment, it is shown that the optimization factor is converged to the true value in the proposed IO-CSI and MR-IO-CSI method, and the inversion results are as good as those of the conventional CSI and MR-CSI method without incident field distortion. The measured data inversion results of Fresnel experiment demonstrate the ability of the single and multifrequency IO-CSI and MR-IO-CSI methods to solve practical inverse problems. This method can be applied to situations where the calibration factor is hard to obtain.

Data Availability

Previously reported [TXT] data were used to support this study and are available at (https://doi.org/10.1088/0266-5611/21/6/S09). The datasets are used in part (Results and Discussion—the Fresnel measurement data) in this manuscript to verify the proposed inversion method. Also, the datasets are cited in this manuscript (Results and Discussion—the Fresnel measurement data) within the text as references [16].

Conflicts of Interest

The authors declare that they have no conflicts of interest.

Acknowledgments

This work was supported by the National Natural Science Foundation of China (grant nos. U1633202 and 61731007).

References

[1] P. M. Berg and R. E. Kleinman, "A contrast source inversion method," *Inverse Problems*, vol. 13, no. 6, pp. 1607–1620, 1997.

[2] P. M. Berg, A. L. V Broekhoven, and A. Abubakar, "Extended contrast source inversion," *Inverse Problems*, vol. 15, no. 5, pp. 1325–1344, 1999.

[3] P. M. van den Berg and A. Abubakar, "Contrast source inversion method: state of art," *Progress in Electromagnetics Research*, vol. 34, pp. 189–218, 2001.

[4] T. Isernia, L. Crocco, and M. D'Urso, "New tools and series for forward and inverse scattering problems in lossy media," *IEEE Geoscience and Remote Sensing Letters*, vol. 1, no. 4, pp. 327–331, 2004.

[5] M. D'Urso, T. Isernia, and A. F. Morabito, "On the solution of 2-D inverse scattering problems via source-type integral equations," *IEEE Transactions on Geoscience and Remote Sensing*, vol. 48, no. 3, pp. 1186–1198, 2010.

[6] X. Chen, "Subspace-based optimization method for solving inverse-scattering problems," *IEEE Transactions on Geoscience and Remote Sensing*, vol. 48, no. 1, pp. 42–49, 2009.

[7] X. Chen, *Computational Methods for Electromagnetic Inverse Scattering*, John Wiley & Sons, Hoboken, NJ, USA, 2018.

[8] S. Sun, B. J. Kooij, T. Jin, A. G. Yarovoy, and A. G. Yarovoy, "Cross-correlated contrast source inversion," *IEEE Transactions on Antennas and Propagation*, vol. 65, no. 5, pp. 2592–2603, 2017.

[9] S. Sun, B.-J. Kooij, A. G. Yarovoy, and A. G. Yarovoy, "Inversion of multifrequency data with the cross-correlated contrast source inversion method," *Radio Science*, vol. 53, no. 6, pp. 710–723, 2018.

[10] A. Abubakar, W. Hu, P. M. van den Berg, and T. M. Habashy, "A finite-difference contrast source inversion method," *Inverse Problems*, vol. 24, no. 6, Article ID 065004, 2008.

[11] A. Abubakar, G. Pan, M. Li, L. Zhang, T. M. Habashy, and P. M. van den Berg, "Three-dimensional seismic full-waveform inversion using the finite-difference contrast source inversion method," *Geophysical Prospecting*, vol. 59, no. 5, 2011.

[12] A. Zakaria, C. Gilmore, and J. LoVetri, "Finite-element contrast source inversion method for microwave imaging," *Inverse Problems*, vol. 26, no. 11, Article ID 115010, 2010.

[13] A. Zakaria and J. LoVetri, "The finite-element method contrast source inversion algorithm for 2D transverse electric vectorial problems," *IEEE Transactions on Antennas and Propagation*, vol. 60, no. 10, pp. 4757–4765, 2012.

[14] H. Li, L. Chen, and J. Qiu, "Convolutional neural networks for multifrequency electromagnetic inverse problems," *IEEE Antennas and Wireless Propagation Letters*, vol. 20, no. 8, pp. 1424–1428, 2021.

[15] R. F. Bloemenkamp, A. Abubakar, and P. M. Berg, "Inversion of experimental multi-frequency data using the contrast source inversion method," *Inverse Problems*, vol. 17, no. 6, pp. 1611–1622, 2001.

[16] J.-M. Geffrin, P. Sabouroux, and C. Eyraud, "Free space experimental scattering database continuation: experimental set-up and measurement precision," *Inverse Problems*, vol. 21, no. 6, pp. S117–S130, 2005.

[17] M. Ostadrahimi, P. Mojabi, C. Gilmore et al., "Analysis of incident field modeling and incident/scattered field calibration techniques in microwave tomography," *IEEE Antennas and Wireless Propagation Letters*, vol. 10, pp. 900–903, 2011.

[18] C. Narendra, I. Jeffrey, and P. Mojabi, "Using the source reconstruction method to model incident fields in microwave tomography," *IEEE Antennas and Wireless Propagation Letters*, vol. 16, pp. 46–49, 2017.

[19] L. Crocco and T. Isernia, "Inverse scattering with real data: detecting and imaging homogeneous dielectric objects," *Inverse Problems*, vol. 17, no. 6, pp. 1573–1583, 2001.

[20] R. Palmeri, M. T. Bevacqua, A. F. Morabito, and T. Isernia, "Design of artificial-material-based antennas using inverse scattering techniques," *IEEE Transactions on Antennas and Propagation*, vol. 66, no. 12, pp. 7076–7090, 2018.